



Research Article

In situ study on the oscillation of mobile droplets and force analysis during the directional solidification of Al-Bi alloy

Ya Zhang^a, Yue Wu^a, Yang Tang^a, Jianbo Ma^b, Bo Mao^a, Yanling Xue^b, Hui Xing^{a,c,*}, Jiao Zhang^{a,c,*}, Baode Sun^{a,c}

^aShanghai Key Lab of Advanced High-temperature Materials and Precision Forming and State Key Lab of Metal Matrix Composites, Shanghai Jiao Tong University, Shanghai 200240, China

^bShanghai Synchrotron Radiation Facility, Shanghai Advanced Research Institute, CAS, Shanghai 201204, China

^cCollaborative Innovation Center for Advanced Ship and Deep-sea Exploration, Shanghai Jiao Tong University, Shanghai 200240, China

ARTICLE INFO

Article history:

Received 2 April 2023

Revised 12 June 2023

Accepted 12 June 2023

Available online 3 September 2023

Keywords:

Radiography

Solidification

Immiscible alloys

Droplet behavior

Solid/liquid interface

ABSTRACT

During solidifications of immiscible alloys, the motion of droplets at the solid/liquid (S/L) interface is generally driven by dragging force, gravity force, repulsion force of interface, and thermal-solutal Marangoni force. However, there is few *in situ* study investigating kinetics behavior to analyze the forces on droplets. The mechanism of droplet motion remains unclear due to the unavailability or uncertainty of the effect of convection and solutal Marangoni force on droplet behavior. In this study, directional solidification of immiscible Al-Bi alloy was observed *via* synchrotron radiography, and the horizontal oscillation of droplets at S/L interface was detected for the first time. Forces, especially solutal Marangoni force, were calculated based on the *in situ* measured radius of droplets and thermal-solutal gradients. The experimental results cannot be reasonably explained by the previous analysis model which neglects melt convection. The non-negligible effect of flow on droplet motion was demonstrated, and the force balance of droplet both vertically and horizontally can be obtained considering a lift force of 6.39×10^{-9} N and a modified solute-related parameter $\frac{d\sigma}{dc}$ of 0.45–0.65 J m⁻², respectively.

© 2024 Published by Elsevier Ltd on behalf of The editorial office of Journal of Materials Science & Technology.

1. Introduction

The mechanical properties of immiscible alloys are significantly affected by the distribution of droplets generated during liquid decomposition or the monotectic reaction in the matrix [1]. The well-dispersed second phase is highly desired in microstructural control. Unfortunately, immiscible alloys tend to segregate seriously during terrestrial casting processes in immiscible gaps due to the gravity and large differences of density between components, deteriorating the practical properties. As for solidifications under microgravity, the Marangoni motion of droplets occurs due to the existence of variation of interfacial tension caused by thermal-solutal gradients around the droplet, leading to collision and coagulation among droplets. Thus, it is necessary to reveal the dynamic mechanism of droplet behavior for better control of second phase dispersion.

The interactions between S/L interface and droplets, including engulfment and repulsion, determine the distribution of particles in solidified structure [2]. The critical velocity between engulfment and repulsion above which droplet is engulfed, mainly depends on the forces on droplets. The forces on droplets at the S/L interface front, including gravity force, viscous force, thermal Marangoni force, and repulsion force of interface, have been investigated by several numerical models [2,3]. He et al. [4] established the kinetic criteria for interactions between droplets and interface during directional solidification of Al-Bi-Cu alloy, as well as studied the phenomenon of dendrites capturing droplets based on the above models [2]. Wei et al. [5] employed the drop tube method and numerical simulation to demonstrate that Marangoni migration plays a dominant role in the aggregation and coalescence of the second phase and formation of core/shell structure during the solidification of Fe-Sn-Ge alloy. Effects of melt convection on the behaviors of droplets have also drawn more attention. Mukherjee et al. [6] investigated the effect of lift force caused by melt convection on droplets at the S/L front via simulation methods. They addressed it is necessary to validate the existing models where melt flow is neglected. Thus, the force analysis model of droplets

* Corresponding authors.

E-mail addresses: xinghui@sjtu.edu.cn (H. Xing), zj119@sjtu.edu.cn (J. Zhang).

which involved the time-resolved parameters including droplet radius and thermal-solutal gradient should be further conducted by *in situ* methods due to the limitations of traditional postmortem analysis or numerical simulation.

Synchrotron radiation X-ray imaging technologies have been widely applied to studying the solidification of immiscible alloys [7–22]. Schaffer et al. [18] observed the motion of droplets at S/L front, and proposed that the solutal Marangoni force might be the reason for droplets not being engulfed by the S/L interface. Lu et al. [17] demonstrated the crucial influence of gravity force, thermal Marangoni force, and dragging force on solidified microstructure. Garcia-Moreno et al. [22] observed the motion of droplets driven by hydrodynamic force, gravity force, melt convection, and Marangoni force through real-time 3D scanning technology. Liotti et al. [23] calculated the flow velocity in mushy zones and the pressure drop caused by volume shrinkage based on the force balance when solutal Marangoni force is not considered. However, solutal Marangoni force was not quantitatively calculated in the above *in situ* studies [17–19,23]. Besides, force analysis on droplets which depends on time-evolved thermal-solutal gradients has not been developed, thus the current force analysis models of droplets need to be further validated.

In this work, we firstly observed the horizontal oscillation of droplets at the S/L front during the solidifications of Al-3.2 wt.% Bi alloy. Solutal Marangoni force and the solute-related parameter $\frac{\partial \sigma}{\partial c}$ were estimated for the first time based on the vertical force balance of droplets. Thus, the horizontal forces on droplets can be calculated and compared with experimental results. The motion of droplets at S/L front was not well consistent with our force analysis model where melt convection was not concerned, while a force balance can be obtained by introducing a lift force caused by flow field, indicating the non-negligible effect of flow on droplet motion. Even though, the perspective and method of *in situ* force analysis can enlighten the follow-up studies on improving the force analysis models.

2. Experimental method

Al-3.2 wt.% Bi alloy was chosen to investigate the directional solidification, and monotectic reaction $L_1 \rightarrow L_2 + S$ occurs as cooled at $T_M = 658$ °C, where L_1 is Al-rich liquid phase with 0.5 wt.% Bi,

L_2 is Bi-rich liquid phase with 97 wt.% Bi and S is solid phase with 0.2 wt.% Bi [24]. The alloy was prepared by melting high-purity Al and Bi in a graphite crucible coated with boron nitride. Thin polished foil samples (~ 250 μm) were sandwiched with two Al_2O_3 sheets with a size of $50 \times 15 \times 0.125$ mm, and sealed together with a silica thread to avoid oxidation. Alloy was heated over liquidus temperature and homogenized for several minutes under thermal gradient ∇T_Y of 109 K/cm, and then cooled at a constantly low undercooling rate R of 10 K/min to focus on dynamics during solidification. Other solidification configurations with $\nabla T_Y = 109$ K/cm, $R = 20$ K/min, and $\nabla T_Y = 187$ K/cm, $R = 20$ K/min were also performed by remelting the sample, each experiment was performed once to diminish the oxide of sample. *In situ* synchrotron X-ray radiography studies of the solidification of Al-3.2 wt.% Bi were carried out at the 13HB beamline at the Shanghai Synchrotron Radiation Facility (SSRF) in China, with a monochromatic X-ray energy of 20 KeV based on a double crystal monochromator. The detector was composed of a Hamamatsu ORCA-Flash 4.0 V2 sCMOS detector and an Optique Peter X-ray beam imaging microscope equipped with $2 \times$ lenses. Spatial resolution is 3.25 $\mu\text{m}/\text{pixel}$, the size of the field of view (FOV) is 4.2×7.4 mm and the frame rate is 6.7 fps. The comprehensive description of the experimental setup can be found in Refs [25,26].

Solute concentration $C_{X,Y}(t,X,Y)$ and its derivative, which is recognized as concentration gradient $\nabla C_{X,Y}(t,X,Y)$ near the droplet is obtained from flat-corrected images with Beer Lambert law [25–28]. Concentration in liquid and mushy zone is obtained with Eqs. (1) and (2) and the details of derivation are shown in Appendix. The meanings of symbols are listed in Table 1. The solutal gradient is obtained with Eq. (3). The errors of the obtained liquid solute concentration were mainly introduced by the set values of the densities during this procedure [29]. The relative error of solute content is less than $7.9 \times 10^{-5}\%$. The relative error of solutal gradient is 0.34%.

$$C_l(t, X, Y) = C_0 + \frac{\ln(I_l) - \ln(I_{\text{ref}})}{\delta \left[\left(\frac{\mu}{\rho} \right)_{\text{Al}} \rho_{\text{Al},l} - \left(\frac{\mu}{\rho} \right)_{\text{Bi}} \rho_{\text{Bi},l} \right]} \quad (1)$$

Table 1
List of symbols.

Symbol	Value	Unit	Meaning
a_0	2.86×10^{-10}	m	Atomic diameter of Al
C_A	0.5 [6]		Coefficient for the virtual added mass
g	9.8	m s^{-2}	Gravity acceleration
n	7 [35]		A positive integer between 2 and 7
R_x	8.31441	$\text{J mol}^{-1} \text{K}^{-1}$	Gas constant
T_c	1310	K	Critical temperature
$(\mu/\rho)_{\text{Al}}$	3.441	cm^2/g	Mass attenuation coefficient for Al at 20 KeV
$(\mu/\rho)_{\text{Bi}}$	89.52	cm^2/g	Mass attenuation coefficient for Bi at 20 KeV
$\rho_{\text{Al},l}$	2.375	g/cm^3	Density of liquid Al
$\rho_{\text{Al},s}$	2.71	g/cm^3	Density of solid Al
$\rho_{\text{Bi},l}$	9.42	g/cm^3	Density of liquid Bi
$\rho_{\text{Bi},s}$	9.72	g/cm^3	Density of solid Bi
k_m	238 [38,39]	$\text{W K}^{-1} \text{m}^{-1}$	Thermal conductivity of L_1
k_β	15.5 [38,40]	$\text{W K}^{-1} \text{m}^{-1}$	Thermal conductivity of L_2
ρ_m	2340 [34]	kg m^{-3}	Density of L_1
ρ_β	9550 [34]	kg m^{-3}	Density of L_2
$\Delta\rho$	7210 [34]	kg m^{-3}	Density difference
$\bar{\eta}$	η_β/η_m		Droplet viscosity / matrix viscosity

$$C_s(t, X, Y) = \frac{C_0 \left(\frac{\mu}{\rho} \right)_{\text{Bi}} \rho_{\text{Bi},1} - C_0 \left(\frac{\mu}{\rho} \right)_{\text{Al}} \rho_{\text{Al},1} + \left(\frac{\mu}{\rho} \right)_{\text{Al}} \rho_{\text{Al},1} - \left(\frac{\mu}{\rho} \right)_{\text{Al}} \rho_{\text{Al},s} - \frac{\ln(I_s) - \ln(I_{\text{ref}})}{\delta}}{\left(\frac{\mu}{\rho} \right)_{\text{Bi}} \rho_{\text{Bi},s} - \left(\frac{\mu}{\rho} \right)_{\text{Al}} \rho_{\text{Al},s}} \quad (2)$$

$$\nabla C_{X,Y}(t) = \frac{dC}{dX,Y} \quad (3)$$

Temperature $T_{X,Y}(t,X,Y)$ and temperature gradient $\nabla T_{X,Y}(t,X,Y)$ are obtained with Eqs. (4) and (5), where R is cooling rate, V is growth velocity of solid phase, R/V is the effective temperature gradient imposed on the sample in the Bridgman furnace, d is distance of droplets and the liquid-solid interface with the equilibrium monotectic temperature T_M . Details of derivation of local temperature and thermal gradient are shown in Appendix. The errors of the obtained $T_{X,Y}(t,X,Y)$ and $\nabla T_{X,Y}(t,X,Y)$ were mainly introduced by uncertainty of the interface and dX,Y . The error of local temperature is 0.0108%. The relative error of vertical thermal gradient which stem from location of interface with uncertainty of $\pm 3.25 \mu\text{m}$ is 0.0283%. The error of horizontal thermal gradient is less than 0.55%. Resultant velocity $V(t)$ and force $F(t)$ of the droplet are obtained with Eqs. (6) and (7) after derivation in the first- and second-order of the recorded position variation of droplet ($X(t)$, $Y(t)$).

$$T(t, X, Y) = T_M + \frac{R}{V} d \quad (4)$$

$$\nabla T_{X,Y}(t) = \frac{dT}{dX,Y} \quad (5)$$

$$V_{p,X,Y}(t) = \frac{dX,Y}{dt} \quad (6)$$

$$F_{X,Y}(t) = \rho \frac{4\pi}{3} r_p^3 \frac{dV_{p,X,Y}}{dt} \quad (7)$$

3. Results and discussion

The upward solidification of Al-3.2 wt.% Bi is shown in Fig. 1(a). The growing solid continuously rejected the solute Bi which enriched at the S/L front [30]. The curved shape of interface stems from the horizontal thermal gradient caused by non-uniformity [31,32] of heat transfer of Bridgeman furnace. Thus, solute segregation which is intensified by thermal convection formed in the concave of the interface, and the increased supersaturation of solute there promoted the nucleation and growth of droplets. Simultaneously, collision and coalescence of tiny droplets were facilitated by Brownian motion, Stokes motion and thermal-solutal Marangoni motion [30,33]. Five droplets with a radius of 4.07×10^{-5} m with dark grayscale formed in the field of view (FOV), named a, b, c, d, and e. The radiuses of droplets increased linearly in the solute enriched melt, as shown in Fig. 1(b). The distances between droplets are keeping approximately $320 \mu\text{m}$ with the propagation of S/L interface. Solute Bi is absorbed by adjacent growing droplets constantly, leaving the interlaced Bi-depleted and Bi-rich solid phase behind ($t = 25.95$ s), as shown by the black and yellow arrows in Fig. 1(a2). The horizontal motion of droplets can be clearly seen in Fig. 1(c) and (d1). Moreover, the oscillation of droplets is an intrinsic feature according to the trajectories of droplets in the other two experiments shown in Fig. 1(d2, d3).

The force analysis was further conducted based on the previous models [23,34,35] to explain the motion of droplets, which involves solutal Marangoni force F_{CM} , thermal Marangoni force F_{TM} , gravity force F_g , repulsion force of interface F_I , and viscous

force F_V , virtual mass force F_{VM} [6], as shown in Fig. 2. The computational formulas are shown as Eqs. (8–16), where distance between droplet and interface d , droplet radius r and droplet velocity μ and interface curvature radius R_I is obtained from radiographic images, other parameters are listed in Table 1.

$$F_{\text{CM}} = -\frac{4\pi \eta_m k_m r^2}{(\eta_m + \eta_\beta)(2k_m + k_\beta)} \cdot \frac{\partial \sigma}{\partial C} \cdot \nabla C \quad (8)$$

$$F_{\text{TM}} = -\frac{4\pi \eta_m k_m r^2}{(\eta_m + \eta_\beta)(2k_m + k_\beta)} \cdot \frac{\partial \sigma}{\partial T} \cdot \nabla T \quad (9)$$

$$F_g = \frac{4\pi}{3} r^3 \Delta \rho \cdot g \quad (10)$$

$$F_I = 2\pi r \cdot (\sigma_{\beta-s} - \sigma_{\beta-l}) \left(\frac{a_0}{a_0 + d} \right)^n \cdot \psi \quad (11)$$

$$\psi = \frac{64r^2 R_I^3 (R_I - r - a_0 - d)}{(a_0 + d + 2r)^2 (a_0 + d - 2R_I)^2 (a_0 + d - 2R_I + 2r)^2} \quad (12)$$

$$F_V = 6\pi \eta \mu r \quad (13)$$

$$F_{\text{VM}} = -C_A \frac{4\pi}{3} \rho_l r_p^3 \frac{dV_p}{dt} \quad (14)$$

$$F_X = F_{X-\text{TM}} + F_{X-\text{CM}} + F_{X-V} + F_{X-\text{VM}} \quad (15)$$

$$F_Y = F_{Y-\text{TM}} + F_{Y-\text{CM}} + F_{Y-\text{VM}} + F_I + F_{Y-V} + F_g \quad (16)$$

where η_m and η_β (N s m^{-2}) is viscosity of pure Al [36] and pure Bi [37] shown in Eqs. (17) and (18). $\frac{\partial \sigma}{\partial C}$ is temperature-dependent term for surface tension shown in Eq. (19).

$$\eta_m = 10^{-3} \times 0.149 \times e^{1000 \times 16.5 / (R_X \times T)} \quad (17)$$

$$\eta_\beta = 10^{-3} \times 0.4458 \times e^{1000 \times 6.45 / (R_X \times T)} \quad (18)$$

$$\frac{\partial \sigma}{\partial T} = -\delta \cdot \sigma_0 \cdot \frac{1}{T_c} \cdot \left(1 - \frac{T}{T_c} \right)^{(\delta-1)} \quad (19)$$

3.1. Thermal-solutal gradients near droplets

The vertical solute concentration C_Y near droplets ($t = 17.40$ s) is shown in Fig. 3(a), and the relative position of droplets is referring to that of droplet a. The local concentration reduced with the increase of distance from droplets. The vertical solutal gradients ranged from 3.3 to 4.7 wt.%/m ($t = 17.40$ –25.95 s).

The solute near droplets is trapped by propagated mushy solid during solidification. The trapped solute concentration in melt corresponded to the concentration in solid at zone 1 ($t = 25.95$ s), as shown in Fig. 1(a2). The solute concentration near droplets was described by ∇C_Y in solid rather than that in melt due to the difficulty in measuring the fast evolved concentration on the moving paths of droplets. Averaging the concentration C_X along horizontal direction can be seen in Fig. 3(b), with the positions of five droplets being indicated by red lines. For the convenience of calculation, the fitting curve of the peak values C_{Max} denotes the

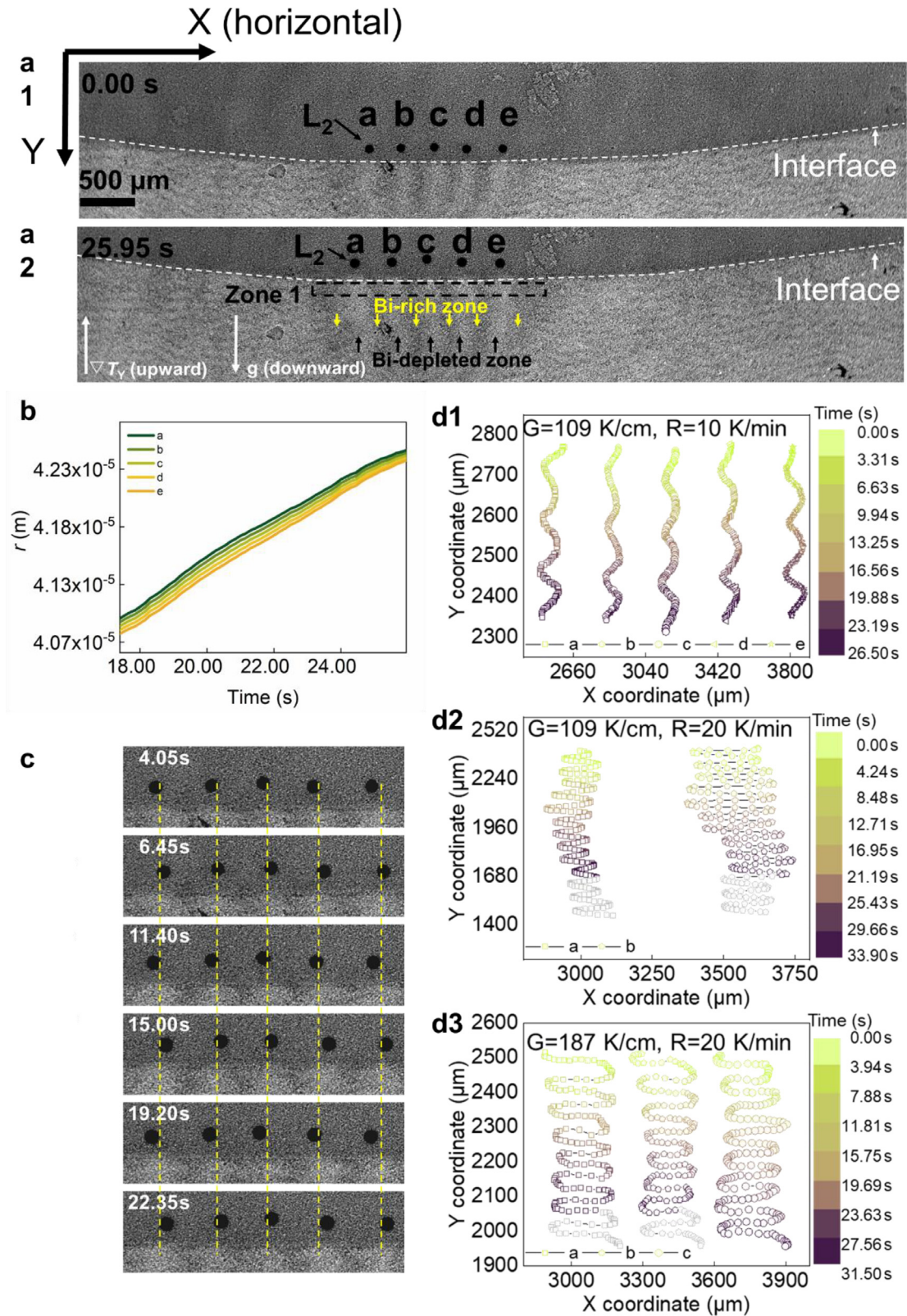


Fig. 1. (a) Radiograph sequence of the upward solidification of Al-3.2Bi with temperature gradient ∇T_Y of 109 K/cm and cooling rate R of 10 K/min, where droplet and solid are in dark and light grayscale, respectively. Rightward and downward is defined as positive direction of X and Y axis, respectively. Evolution of (b) radius and (c) position of droplets during $t=4.05$ –22.35 s. Oscillated trajectories of droplets under (d1) $\nabla T_Y=109$ K/cm, $R=10$ K/min, (d2) $\nabla T_Y=109$ K/cm, $R=20$ K/min, and (d3) $\nabla T_Y=187$ K/cm, $R=20$ K/min.

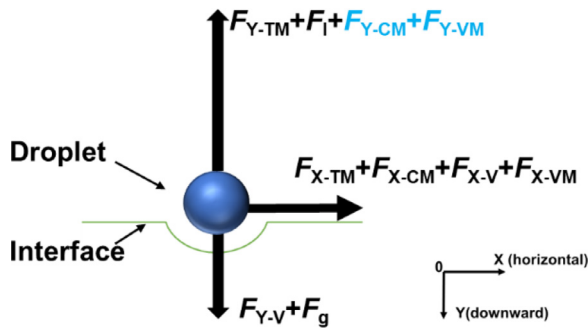


Fig. 2. Schematic of forces acting on droplet in front of the S/L interface, where forces with uncertain direction are in blue text.

horizontal solute distribution at the S/L front. Along the horizontal direction, the solute concentration increases first and then de-

creases after crossing the lowest position of S/L interface, while the absolute solutal gradient ∇C_X is opposite, as shown in Fig. 3(c). Similarly, the absolute thermal gradient value along horizontal direction tended to decrease first and then increase, as shown in Fig. 3(d, e). Note that the error bars were not added to ensure the clarity of the plotted data since the profiles overlapped. The relevant error analysis was shown in Experimental method.

3.2. Estimation of solute-related parameter $\frac{\partial \sigma}{\partial c}$

The vertical resultant force and F_{Y-VM} on droplets can be approximately deduced as zero with Eqs. (7) and (14) based on the nearly constant vertical velocity which is shown in Fig. 4(a). The magnitude of viscous force, gravity force, and thermal Marangoni force are deduced as 10^{-11} , 10^{-8} , and 10^{-9} N with Eq. (13), Eq. (10) and Eq. (9), respectively, as shown in Fig. 4(b–d). The repulsion force of interface with a magnitude of 10^{-45} N, calcu-

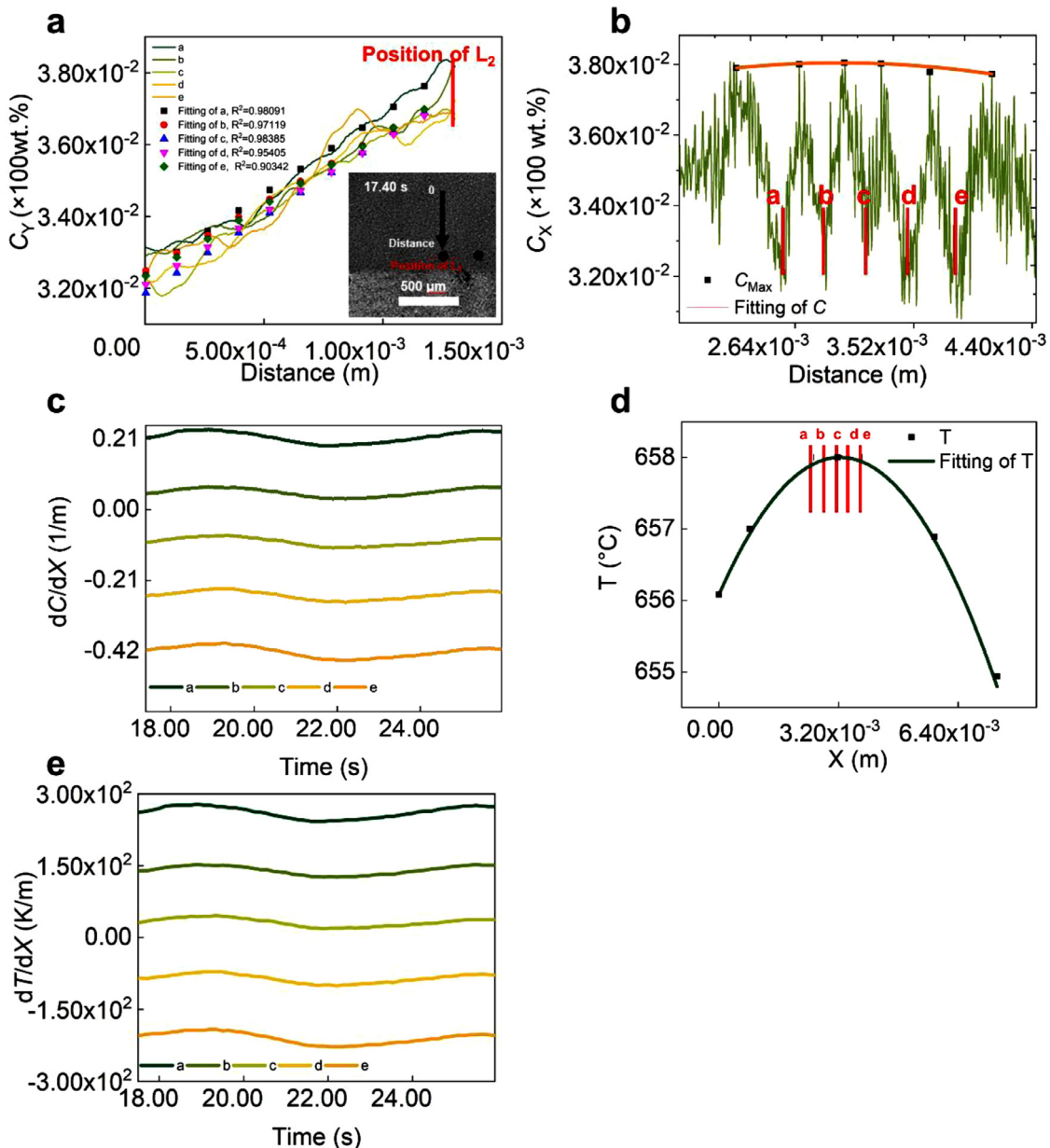


Fig. 3. Variables near droplets as a function of time. Vertical (a) C_Y . Horizontal (b) C_X and (c) ∇C_X and (d) T_X and (e) ∇T_X . ∇C and ∇T are positive when parallel to the gravity force.

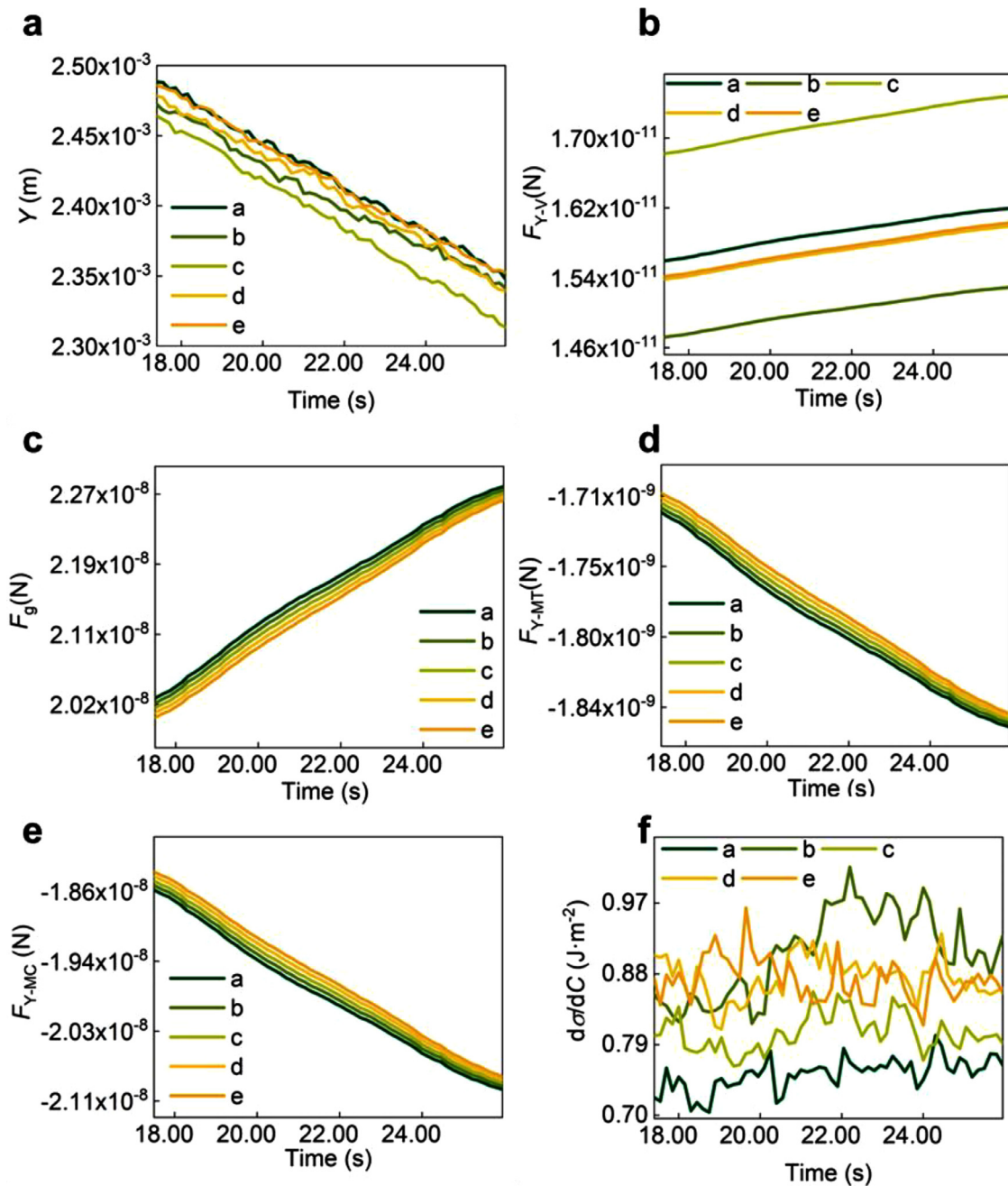


Fig. 4. (a) Vertical positions of droplets and (b–e) F_{Y-V} , F_g , F_{Y-MT} , F_{Y-CM} forces on droplet. (f) Solute-related parameter $\frac{d\sigma}{dC}$.

lated by Eq. (11) with distance between droplet and interface d ($117 \mu\text{m}$) and the radius ($0.022\text{--}0.026 \text{ m}$) of curvature of S/L interface, can be neglected. Thus, there must exist the non-negligible solutal Marangoni force along the vertical direction to balance the above four types of force based on Eq. (16). The evolution of F_{Y-CM} with an opposite direction of solutal gradient can be obtained as shown in Fig. 4(e). Based on the solute concentration near droplets $C=3.8 \text{ wt.}\%$ (Fig. 3(a)) and the according gradient and Fig. 4(e), the $\frac{\partial\sigma}{\partial C}|_{C=3.8\text{wt.}\%}$ can be estimated $0.7\text{--}1.0 \text{ J m}^{-2}$ according to Eq. (8), as shown in Fig. 4(f).

3.3. Horizontal oscillation of droplets

The time-evolved horizontal velocities and resultant forces shown in Fig. 5(a,b) were measured and calculated based on the

radiograph sequence in Fig. 1(c). The magnitudes of oscillating velocities and resultant forces are deduced as 10^{-5} m/s and 10^{-13} N with Eqs. (6) and (7), respectively. As for the component forces, the magnitudes of F_{X-TM} and F_{X-V} , F_{X-VM} are 10^{-11} , 10^{-11} , and 10^{-14} N based on the Eqs. (9), (13) and (14), respectively, as shown in Fig. 5(c–e). Thus, the magnitude of the solutal Marangoni force should be 10^{-11} N to balance force ($F_X - (F_{X-TM} + F_{X-V} + F_{X-VM})$) shown in Fig. 5(f) based on Eq. (15), to meet the resultant force F_X . The schematic of solute distribution between droplets based on Ref. [18] and Fig. 3(e) is shown in Fig. 5(g). The solute near droplets 1, 2, and 3 is absorbed continuously, resulting in the sinusoidal distribution between droplets. Note that “sinusoidal” is just the feature of solute profile instead of the strict sinusoidal curve. The solute concentrations in zones Z2 and Z3 near droplet 2 are higher than that in zones Z1 and Z4 due to the solute enrich-

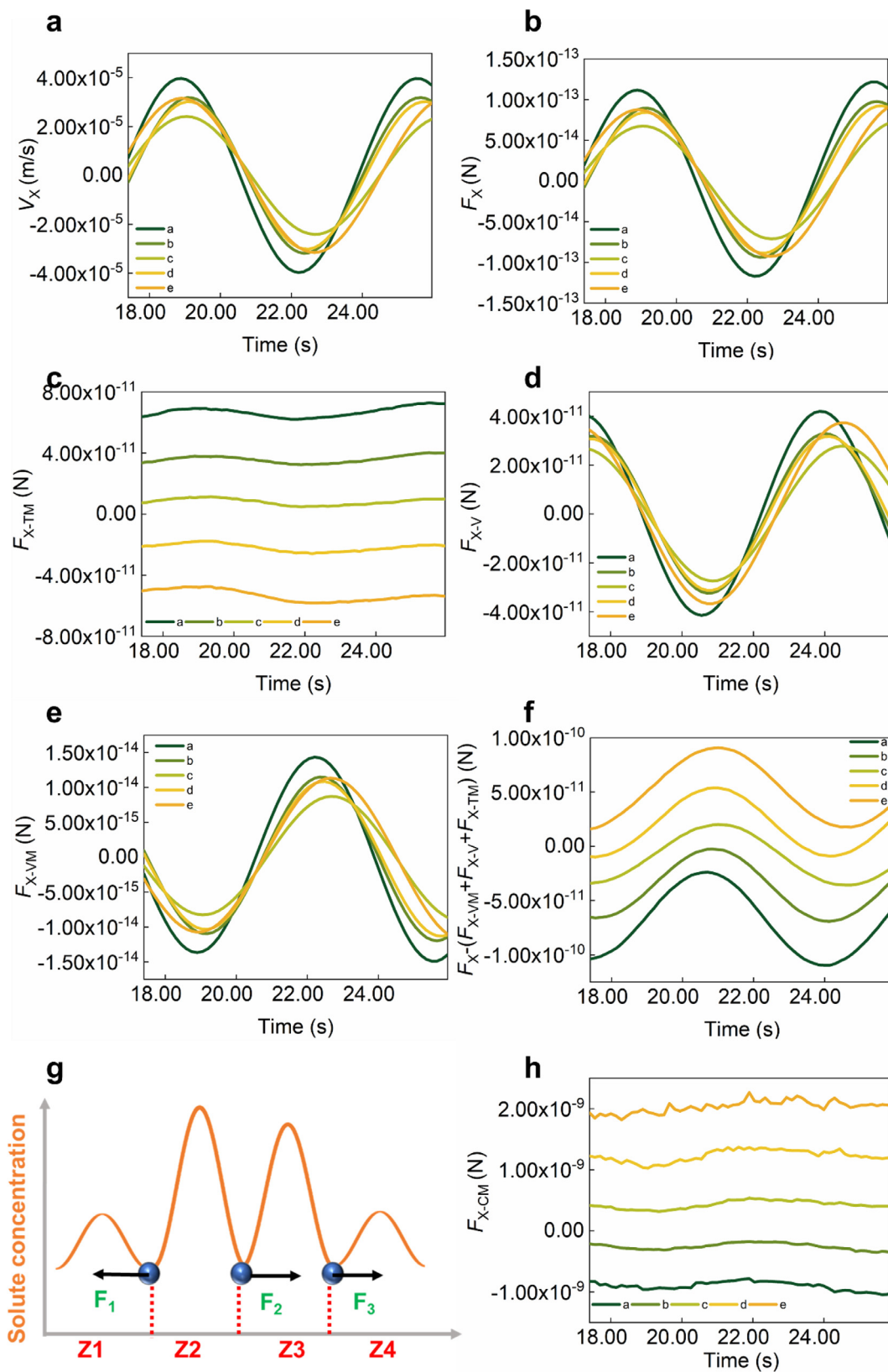


Fig. 5. (a–f) Horizontal velocity V_{X-TM} , resultant force F_X , F_{X-TM} , F_{X-V} , F_{X-VM} , $F_X - (F_{X-TM} + F_{X-V} + F_{X-VM})$ of droplet. (g) Schematic of inter-droplet solute profile in zones Z1, Z2, Z3, Z4 and F_{X-CM} of droplet named 1, 2, 3. (h) F_{X-CM} of droplet.

ment at the lowest position of the curved S/L interface. The solutal Marangoni force balances the F_{X-V} and F_{X-TM} to prevent droplets from collision. Whereas, the magnitude of F_{X-CM} calculated by the above $\frac{\partial\sigma}{\partial C}$ and horizontal solutal gradient in Fig. 3(d) and Eq. (8) is 10^{-10} – 10^{-9} N (Fig. 5(h)), which relatively largely differs from that of F_X ($F_{X-TM} + F_{X-V} + F_{X-VM}$). This disagreement proves the limitation of models that neglects melt convection.

Both curved isotherms and volume change result in horizontal melt flow during solidifications [41]. Velocity boundary of melt exists near the S/L interface due to the viscous force caused by the interface and crucible wall, which means that the intensities of melt flow are different in local area. The impact of Basset force which stems from the history of relative velocity between droplet and melt on the motion of droplets during melt flow is negligible [42,43]. However, based on the study of Stefanescu et al. [6,43,44], the effect of lift force caused by convection on the motion of droplets should be considered which increase the critical velocity for engulfment of droplets as the gravity level increases. Besides, the effect of lift force on the motion of relatively large droplets ($>10 \mu\text{m}$) or particles was also addressed in another previous study [45]. The magnitude of lift force on droplets with a radius r of $40 \mu\text{m}$ in our work can be estimated as 6.39×10^{-9} N according to the proportional relation between lift force and r^2 [46]. Thus, the magnitude of modified $F_{Y-CM} = F_g - F_{Y-V} - F_{Y-TM}$ is 1.18×10^{-8} N and the corresponding $\frac{\partial\sigma}{\partial C}$ decreases to 0.45 – 0.65 J m^{-2} , which is consistent with measured value of 0.889 and 0.9 J m^{-2} for Al–Fe and Al–Ni alloy respectively [47]. F_{X-CM} is thus corrected to 2.95×10^{-10} N, and then the horizontal F_X ($F_{X-TM} + F_{X-V} + F_{X-VM}$) in Fig. 5(f) can be balanced.

4. Conclusion

Droplets nucleate and grow continuously at the S/L front where solute accumulates during the directional solidification of Al–3.2 wt.% immiscible alloy. The interlaced Bi-depleted and Bi-rich solid phases form due to the absorption of Bi by neighboring droplets. Droplets move upward constantly with a velocity of 10^{-5} m/s. The vertical motion of droplets is strongly impacted by gravity force and thermal Marangoni force, while the effect of pushing force of interface and viscous force can be neglected. The $\frac{\partial\sigma}{\partial C}|_{C=3.8\text{wt.}\%}$ is estimated as 0.7 – 1 J m^{-2} based on the force balance. The horizontal oscillation of droplets is affected by thermal Marangoni force and viscous force with a magnitude of 10^{-11} N. The existence of solutal Marangoni force prevents droplets from collision. Current models cannot reasonably explain the motion of droplets at the S/L interface. Force balance of droplet is likely achieved by introducing an additional lift force of 6.39×10^{-9} N

$$C_s(t, X, Y) = \frac{C_0 \left(\frac{\mu}{\rho}\right)_{\text{Bi}} \rho_{\text{Bi},l} - C_0 \left(\frac{\mu}{\rho}\right)_{\text{Al}} \rho_{\text{Al},l} + \left(\frac{\mu}{\rho}\right)_{\text{Al}} \rho_{\text{Al},l} - \left(\frac{\mu}{\rho}\right)_{\text{Al}} \rho_{\text{Al},s} - \frac{\ln(I_s) - \ln(I_{\text{ref}})}{\delta}}{\left(\frac{\mu}{\rho}\right)_{\text{Bi}} \rho_{\text{Bi},l} - \left(\frac{\mu}{\rho}\right)_{\text{Al}} \rho_{\text{Al},s}} \quad (\text{A5})$$

and a modified $\frac{\partial\sigma}{\partial C}$ of 0.45 – 0.65 J m^{-2} . Our work reveals that the effect of solutal Marangoni force and lift force on the motion of droplets cannot be ignored. It is necessary to establish a new model that considers solutal Marangoni force and the impact of nonuniform melt flow field. The perspective of this *in situ* study on force analysis can assist the modification of force analysis models in future.

Declaration of Competing Interests

The authors declare that they have no known competing financial interests or personal relationships that could have appeared to influence the work reported in this paper.

Acknowledgments

This work was financially supported by the National Natural Science Foundation of China (Nos. 52271036 and 51971237), and the Shanghai Pujiang Program (No. 21PJ030). The experiments were carried out at BL13HB1 (used to be BL13W1), BL13SSW and USAX beamline at Shanghai Synchrotron Radiation Facility (SSRF).

Appendix

Measurement of solutal concentration

Raw sequences were flat field corrected with a reference frame which represents the homogenous melt of alloy, to remove the effect of the dust on the detector and the effect of the nonuniform intensity bring by the light beam. The relationship between pixel intensity I and content C in various phases is shown in Eqs. (A1)–(A3) based on the Beer-lambert law [27], where I_0 , I_{ref} , I_l and I_s respectively denote the intensity of incident X-ray, homogeneous melt, liquid phase and solid phase. C_0 , C_l and C_s respectively denote the nominal composition of alloy and the solute content in liquid phase and solid phase. Finally, the content of solute in various phases is transferred with the pixel intensity with Eqs. (A4) and (A5), where δ the sample thickness, $(\mu/\rho)_{\text{Al}}$ and $(\mu/\rho)_{\text{Bi}}$ the mass attenuation coefficient for Al and Bi, $\rho_{\text{Al},l}$ and $\rho_{\text{Bi},l}$ the density of liquid Al and Bi, while $\rho_{\text{Al},s}$ and $\rho_{\text{Bi},s}$ the density of solid Al and Bi.

Please note that the mushy zone was treated as a completely solid even though the Bi-droplet was solidified at eutectic temperature $T = 271.5 \text{ }^\circ\text{C}$ since there were no traces of mobile droplet observed, and it implies the liquid channels between well-developed solid phase are small enough to obstruct the droplet motion. Thus, $\rho_{\text{Al},s}$ is adopted for the determination of solute content in solid phases.

$$-\ln\left(\frac{I_{\text{ref}}}{I_0}\right) = \delta \left[(1 - C_0) \left(\frac{\mu}{\rho}\right)_{\text{Al}} \rho_{\text{Al},l} + C_0 \left(\frac{\mu}{\rho}\right)_{\text{Bi}} \rho_{\text{Bi},l} \right] \quad (\text{A1})$$

$$-\ln\left(\frac{I_l}{I_0}\right) = \delta \left[(1 - C_l) \left(\frac{\mu}{\rho}\right)_{\text{Al}} \rho_{\text{Al},l} + C_l \left(\frac{\mu}{\rho}\right)_{\text{Bi}} \rho_{\text{Bi},l} \right] \quad (\text{A2})$$

$$-\ln\left(\frac{I_s}{I_0}\right) = \delta \left[(1 - C_s) \left(\frac{\mu}{\rho}\right)_{\text{Al}} \rho_{\text{Al},s} + C_s \left(\frac{\mu}{\rho}\right)_{\text{Bi}} \rho_{\text{Bi},l} \right] \quad (\text{A3})$$

$$C_l(t, X, Y) = C_0 + \frac{\ln(I_l) - \ln(I_{\text{ref}})}{\delta \left[\left(\frac{\mu}{\rho}\right)_{\text{Al}} \rho_{\text{Al},l} - \left(\frac{\mu}{\rho}\right)_{\text{Bi}} \rho_{\text{Bi},l} \right]} \quad (\text{A4})$$

1 Measurement of thermal gradient

The thermal gradient is interpolated with the applied temperatures for the hot and cold heaters, and a setting thermal gradient ∇T_Y is obtained as

$$\nabla T_Y = \frac{T_{\text{top}} - T_{\text{bot}}}{d_{\text{gap}}} \quad (\text{A6})$$

where d_{gap} is the gap between the heaters at the top and bottom with a set temperature of T_{top} and T_{bot} . The effective thermal gradient is obtained with Eq. (A7) with the propagation velocity of interface V measured in the radiography sequence,

$$\nabla T_{\text{eff-Y}}(t) = \frac{R}{V} \quad (\text{A7})$$

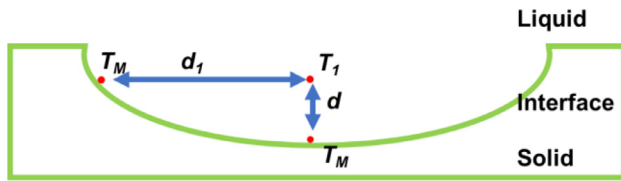


Fig. A1. Sketch of the location and the according temperature around the solid/liquid interface.

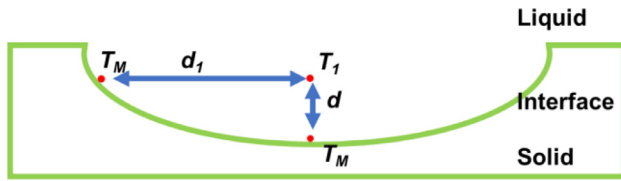


Fig. A1. Sketch of the location and the according temperature around the solid/liquid interface.

where R is cooling rate, V is growth velocity of solid phase.

Then, the local temperature $T(t, X, Y)$ as a function of time t and the location (X, Y) is obtained based on Eq. (A8).

$$T(t, X, Y) = T_M + \frac{R}{V}d \quad (\text{A8})$$

The according horizontal thermal gradient ∇T_X is obtained with Eq. (A9).

$$\nabla T_X(t) = \frac{dT}{dX} = \frac{T_1 - T_M}{d_1} = \frac{Rd}{Vd_1} \quad (\text{A9})$$

where T_M is the thermal invariant monotectic temperature. d and d_1 respectively denote the distance between interface and a position in melt which is denoted as the red dot in Fig. A1. T_1 is the local temperature of the position in melt.

References

- [1] L. Ratke, S. Diefenbach, *Mater. Sci. Eng. R* 15 (1995) 263–347.
- [2] B. Dutta, M.K. Surappa, *Metall. Mater. Trans. A* 29 (1998) 1329–1339.
- [3] D. Shangguan, S. Ahuja, D.M. Stefanescu, *Metall. Trans. A* 23 (1992) 669–680.
- [4] J. He, J.Z. Zhao, X.F. Wang, Q.X. Zhang, H.L. Li, G.Y. Chen, *Acta Metall. Sin.* 43 (2007) 561–566.
- [5] Y.H. Wu, W.L. Wang, Z.C. Xia, B. Wei, *Comput. Mater. Sci.* 103 (2015) 179–188.
- [6] S. Mukherjee, D.M. Stefanescu, *Metall. Mater. Trans. A* 35 (2004) 613–621.
- [7] W. Lu, S. Zhang, W. Zhang, Q. Hu, J. Yu, Y. Fu, J. Li, *Metall. Mater. Trans. A* 48 (2017) 2701–2705.
- [8] M.G.C. Xavier, R.A.V. Reyes, L.F. Gomes, J.E. Spinelli, N. Mangelinck Noël, H. Nguyen Thi, G. Reinhart, *J. Cryst. Growth* 536 (2020) 125592.
- [9] W. Lu, S. Zhang, W. Zhang, G. Kaptay, J. Yu, Y. Fu, J. Li, *Scr. Mater.* 102 (2015) 19–22.
- [10] W. Lu, Q. Hu, W. Zhang, J. Li, *J. Mol. Liq.* 320 (2020) 114478.
- [11] S.D. Imhoff, P.J. Gibbs, M.R. Katz, T.J. Ott, B.M. Patterson, W.-K. Lee, K. Fezzaa, J.C. Cooley, A.J. Clarke, *Mater. Chem. Phys.* 153 (2015) 93–102.
- [12] W. Lu, S. Zhang, W. Zhang, J. Li, *J. Mater. Sci. Technol.* 32 (2016) 1321–1325.
- [13] P.L. Schaffer, R.H. Mathiesen, L. Arnberg, *Mater. Sci. Forum* 649 (2010) 149–158.
- [14] P.L. Schaffer, R.H. Mathiesen, L. Arnberg, M. Di Sabatino, A. Snigirev, *New J. Phys.* 10 (2008) 053001.
- [15] J. Zhu, T. Wang, F. Cao, Y. Fu, H. Xie, T. Xiao, *J. Phys. Conf.* 463 (2013) 012036.
- [16] W.Q. Lu, S.G. Zhang, J.G. Li, *IOP Conf. Ser. Mater. Sci. Eng.* 117 (2016) 012023.
- [17] W.Q. Lu, S.G. Zhang, Q.D. Hu, J.G. Li, *Mater. Lett.* 182 (2016) 351–354.
- [18] P.L. Schaffer, R.H. Mathiesen, L. Arnberg, *Acta Mater.* 57 (2009) 2887–2895.
- [19] P.L. Schaffer, R.H. Mathiesen, L. Arnberg, *Trans. Indian Inst. Met.* 62 (2009) 437–442.
- [20] W.Q. Lu, S.G. Zhang, J.G. Li, *Acta Metall. Sin. Engl. Lett.* 29 (2016) 800–803.
- [21] H.J. Kang, P. Zhou, F. Cao, J. Zhu, Y.-N. Fu, W.X. Huang, T.Q. Xiao, T.M. Wang, *Acta Metall. Sin. Engl. Lett.* 28 (2015) 940–945.
- [22] F. Garcia-Moreno, P.H. Kamm, T.R. Neu, F. Bulck, M.A. Noack, M. Wegener, N. von der Eltz, C.M. Schlepütz, M. Stamparoni, J. Banhart, *Adv. Mater.* 33 (2021) 2104659.
- [23] E. Liotti, A. Lui, T. Connolly, P.S. Grant, *Acta Mater.* 240 (2022) 118298.
- [24] A.J. McAlister, *Bull. Alloy Phase Diagr.* 5 (1984) 247–250.
- [25] Y. Wu, Y. Tang, Y. Zhang, Y. Fu, H. Xing, J. Zhang, J. Jiang, B. Sun, *J. Mater. Sci. Technol.* 122 (2022) 33–43.
- [26] Y. Tang, Y. Wu, Y. Zhang, Y. Dai, Q. Dong, Y. Han, G. Zhu, J. Zhang, Y. Fu, B. Sun, *Acta Mater.* 212 (2021) 116861.
- [27] W.U. Mirihanage, K.V. Falch, I. Snigireva, A. Snigirev, Y.J. Li, L. Arnberg, R.H. Mathiesen, *Acta Mater.* 81 (2014) 241–247.
- [28] D.F. Swinehart, *J. Chem. Educ.* 39 (1962) 333.
- [29] N. Wang, Y. Tang, Y. Wu, Y. Zhang, Y. Dai, J. Zhang, R. Zhang, Y. Xu, B. Sun, *Mater. Charact.* 181 (2021) 111451.
- [30] H. Jiang, Q. Sun, J. Zhao, Z. Yang, *Chin. J. Space Sci.* 36 (2016) 450–454.
- [31] Y. Xu, D. Casari, Q. Du, R.H. Mathiesen, L. Arnberg, Y. Li, *Acta Mater.* 140 (2017) 224–239.
- [32] A.G. Murphy, W.U. Mirihanage, D.J. Browne, R.H. Mathiesen, *Acta Mater.* 95 (2015) 83–89.
- [33] Z. Yang, Q. Sun, J. Zhao, *Acta Metall. Sin.* 50 (2014) 25–31.
- [34] Q. Sun, H. Jiang, J. Zhao, J. He, *Acta Mater.* 129 (2017) 321–330.
- [35] D. Shangguan, D. Stefanescu, *Metall. Trans. B* 22 (1991) 385–388.
- [36] A.T. Dinsdale, P.N. Quedstedt, *J. Mater. Sci.* 39 (2004) 7221–7228.
- [37] H. Jiang, J. Zhao, J. He, *J. Mater. Sci. Technol.* 30 (2014) 1027–1035.
- [38] W. Li, H. Jiang, L. Zhang, S. Li, J. He, J. Zhao, F. Ai, *Scr. Mater.* 162 (2019) 426–431.
- [39] L. Arnberg, R.H. Mathiesen, *JOM* 59 (2007) 20–26.
- [40] H.X. Jiang, Study of the Continuous Solidification of Monotectic Alloys Under the Effect of Electric Current, University of Chinese Academy of Sciences, 2014 Ph.D. Thesis (in Chinese).
- [41] R.H. Mathiesen, L. Arnberg, *Acta Mater.* 53 (2005) 947–956.
- [42] H. Chen, W. Ding, H. Wei, H. Saxén, Y. Yu, *Materials* 15 (2022) 5461.
- [43] S. Mukherjee, D. Stefanescu, in: P. Rohatgi (Ed.), *Analysis of Liquid Convection Effects on the Pushing-Engulfment Transition*, 2000, pp. 89–100.
- [44] F.R. Juretzko, D.M. Stefanescu, B.K. Dhindaw, S. Sen, P.A. Curreri, *Metall. Mater. Trans. A* 29 (1998) 1691–1696.
- [45] J. Friedrich, C. Reimann, T. Jaus, A. Cröll, T. Sorgenfrei, Y. Tao, J.J. Derby, *J. Cryst. Growth* 475 (2017) 33–38.
- [46] A.V. Bune, S. Sen, S. Mukherjee, A. Catalina, D.M. Stefanescu, *J. Cryst. Growth* 211 (2000) 446–451.
- [47] I. Egly, J. Brillo, D. Holland-Moritz, Y. Plevachuk, *Mater. Sci. Eng.* 495 (2008) 14–18.